Direct numerical simulation of Spatially-Developing Three-Dimensional Turbulent Boundary Layer around the leading-edge of a swept wing

Youcheng Xi* and Song Fu*
Corresponding author: xiyc@mail.tsinghua.edu.cn, fs-dem@tsinghua.edu.cn
* School of Aerospace Engineering, Tsinghua University, Beijing, China

Abstract: Predictive simulation of swept wings, lifting bodies, and high-speed inlets requires turbulence models for three-dimensional turbulent boundary layers (3D TBLs), but most high-fidelity data used for model development still come from canonical or idealized three-dimensional flows. This paper presents a direct numerical simulation (DNS) of a Mach-6 swept blunt leading edge as a model-ready database for a spatially developing high-speed 3D TBL. The flow evolves from a quasi-two-dimensional attachment-line turbulent boundary layer into a skewed downstream boundary layer driven by favorable pressure gradient, curvature, and crossflow. A four-stage CFD procedure combines shock fitting, shock capturing, full transition computation, and refined DNS extraction on a $4801 \times 601 \times 2001$ grid. The database includes local streamline coordinates, wall shear and heat transfer, pressure-gradient history, Reynolds stresses, turbulent-kinetic-energy budgets, spectra, near-wall streak orientation, a wall-parallel speed law, and stress-anisotropy model-error metrics. The main finding is that scalar wall-speed similarity and vector/tensor turbulence statistics separate in this flow. The wall-parallel mean-speed magnitude approximately recovers the classical viscous and logarithmic behavior in inner variables, while the velocity direction, wall-shear direction, coherent structures, and Reynolds stresses retain strong three-dimensional history effects. Downstream acceleration produces persistent streak-orientation lag, Reynolds-stress depletion, collapse of the Townsend structure parameter, turbulent-kinetic-energy production deficit, and scale-selective relaminarization in which large-scale motions are strongly suppressed while skewed thermal-momentum streaks remain. The results give specific validation targets for wall models, nonlinear constitutive relations, Reynolds-stress closures, wall-modeled LES, and data-assisted turbulence models.

Keywords: Direct numerical simulation, Three-dimensional turbulent boundary layer, Law of the wall, CFD database, Turbulence modeling.

1. Introduction

Three-dimensional turbulent boundary layers are common on swept wings, lifting bodies, turbomachinery end walls, inlets, and high-speed vehicles. These are also the flows for which Reynolds-averaged models, wall functions, wall-modeled LES, and data-assisted closures remain unavoidable in design calculations. The central difficulty is not simply the presence of a third mean-velocity component. In a 3D TBL, the external streamline, pressure-gradient vector, wall-shear vector, Reynolds-stress tensor, and coherent structures need not share the same direction. Their misalignment produces crossflow, changes the near-wall turbulence cycle, and introduces history effects that are outside the assumptions of local two-dimensional equilibrium [1, 2].

This difficulty has been recognized since the early wall-similarity studies of three-dimensional turbulent boundary layers. Those studies showed that velocity components do not generally collapse in the same way as in a two-dimensional boundary layer, but they also suggested that a resultant wall-parallel velocity and a resultant friction velocity can retain part of the classical wall scaling [3, 4, 5]. This distinction is important for turbulence modeling. If a scalar wall-speed law survives in a 3D TBL, it can serve as a useful wall constraint; if it does not determine the velocity direction, wall-shear direction, or stress tensor, then separate vector and tensor diagnostics are still required.

Direct numerical simulations have provided a second line of understanding by isolating the non-equilibrium mechanisms of 3D wall turbulence. Spalart [6] studied a flat-plate boundary layer subjected to an oscillating free stream and showed how turbulence can lag a time-dependent three-dimensional distortion. Moin et al. [7] imposed an impulsive transverse pressure gradient in a time-dependent turbulent channel and reported the now-familiar stress depletion and stress–strain misalignment. Lozano-Durán et al. [8] revisited this class of time-dependent flow at higher Reynolds number and connected the depletion to structural changes in wall turbulence. Abe [9] considered a spatially developing shear-driven steady 3D boundary layer and showed that the Townsend structure parameter can fall below its two-dimensional equilibrium value. More recently, Gomez [10] extended related ideas[7, 8] to supersonic time-dependent flow and highlighted that compressibility and thermal correlations introduce additional constraints. These studies define several quantities that a useful 3D TBL database should contain: wall scaling, directional lag, Reynolds-stress anisotropy, turbulent-kinetic-energy budgets, spectra, and heat-flux correlations.

At the same time, they also show what remains missing. Their simplified configurations are designed to isolate particular mechanisms, but the crossflow is imposed by an oscillating external condition, an impulsive transverse pressure gradient, a moving wall, or another idealized device. In a swept leading-edge boundary layer, by contrast, the three-dimensionality is generated by the geometry itself. Turbulence first forms near the attachment line and is then convected into a downstream region where favorable pressure gradient, streamline curvature, wall-shear rotation, and crossflow develop together. The wall-shear and heat-transfer fields, coherent structures, and Reynolds stresses therefore carry a spatial history that cannot be reconstructed from a single local mean profile.

High-speed swept configurations add two further constraints. First, the computation must include the shock layer, wall cooling, density variation, transition route, and the small near-wall scales of turbulence in a spatially developing geometry. Second, the thermal field is tied to the same streaks and Reynolds stresses that transport momentum, so heat fluxes and velocity-temperature correlations cannot be treated as secondary output only. Experiments in such flows remain essential for geometry, transition, and integral validation, but matched Reynolds stresses, spectra, heat fluxes, and budget terms are difficult to obtain at the same stations. Instead, DNS can provide these quantities.

The present work therefore uses DNS of a Mach-6 swept blunt leading edge to build a model-ready database for a realistic high-speed 3D TBL. The configuration is motivated by the attachment-line transition problem studied in [11]; here the focus is the fully turbulent downstream boundary layer and its use for model assessment. The paper addresses three questions:

1. can a resolved DNS of a swept leading edge provide reproducible data for a spatially developing high-speed 3D TBL;
2. does a wall-parallel speed scaling remain useful when the velocity direction, wall shear, and near-wall structures are strongly three-dimensional;
3. which structural, budget, spectral, heat-transfer, and stress-orientation quantities expose limitations of common turbulence closures.

The paper is organized as follows. Section 2 describes the flow configuration and numerical method. The database quantities and diagnostics are shown in Section 3. Section 4 presents the main DNS results and Section 5 discusses implications for turbulence modeling. Section 6 summarizes the main findings.

Table 1: Main flow and DNS parameters. Lengths are dimensional unless noted otherwise.

Quantity	Value	Quantity	Value
M_∞	6.0	Λ	45°
Re_∞	1.8×10^7 m^{-1}	T_w^*	370 K
DNS grid	$4801 \times 601 \times 2001$	$\Delta\eta^+$	$0.4 \sim 3$
$\Delta\xi^+_{\max}$	< 5	$\Delta z^+_{\max}$	< 5

2. Flow configuration and numerical method

2.1 Governing equations and numerical method

The simulations solve the dimensionless compressible Navier–Stokes equations for a calorically perfect gas,

$$\frac{\partial \boldsymbol{q}}{\partial t} + \frac{\partial F_j}{\partial x_j} + \frac{\partial F_j^v}{\partial x_j} = 0, \qquad \boldsymbol{q} = [\rho, \rho u_1, \rho u_2, \rho u_3, E_t]^T . \tag{1}$$

Here $E_t = p/(\gamma-1)+\rho u_i u_i/2$ is the total energy per unit volume, and repeated spatial indices are summed. The viscous terms use Newtonian stresses, Fourier heat flux, $Pr = 0.72$, and Sutherland viscosity. Two solvers are combined because a realistic hypersonic flow around the leading edge must resolve both the shock layer and the turbulent boundary layer. A high-order shock-fitting solver first computes the steady laminar base flow and locates the bow shock accurately. The three-dimensional transition and turbulent computations are then advanced with OPENCFD, a validated shock-capturing solver for high-speed flows [12, 13]. Inviscid fluxes are discretized with a hybrid high-order finite-difference method using a seventh-order upwind scheme in smooth regions and WENO reconstruction near discontinuities. Viscous fluxes use sixth-order central differences, and time advancement uses a third-order Runge–Kutta scheme.

2.2 Swept leading-edge configuration

The geometry is the front part of a delta wing with sweep angle $\Lambda = 45°$. The leading-edge thickness is $2L_4 = 40$ mm and the chordwise length is $L_1 = 200$ mm. The freestream Mach number is $M_\infty = 6.0$, the unit Reynolds number is $Re_\infty = 1.8 \times 10^7$ m^{-1}, and the wall is isothermal at $T_w^* = 370$ K. Transition is triggered by a body-fitted isolated roughness element located on the attachment line, representing a realistic sensor- or imperfection-induced route to turbulence rather than an artificial inflow field.

The flow is described in both the body-fitted coordinates (ξ, η, z) and a local streamline coordinate system (S, η, C). The S direction follows the external streamline, C is the wall-parallel crossflow direction, and η is the wall-normal direction. If θ_s denotes the external streamline angle, the streamwise and crossflow velocities are

$$u_s = w \cos\theta_s + u_\xi \sin\theta_s, \qquad u_c = -w \sin\theta_s + u_\xi \cos\theta_s. \tag{2}$$

This coordinate transformation is applied consistently to mean velocities, Reynolds stresses, heat fluxes, and pressure-gradient components. It is not a post-processing convenience only. It is part of the database definition because closure models must learn or predict quantities in a frame that separates the main momentum direction from crossflow effects.

2.3 DNS extraction and grid resolution

The database is produced by a four-stage strategy. First, a two-dimensional shock-fitting computation generates the shock-aligned laminar field. Second, a short three-dimensional shock-capturing pre-computation with periodic spanwise boundary conditions removes interpolation and solver-interface inconsistencies. Third, the full swept leading-edge transition computation is performed with the roughness element and non-reflecting outlets. Fourth, after the flow becomes fully turbulent and statistically homogeneous in the spanwise direction, a downstream subdomain is extracted and recomputed on a refined DNS grid with periodic z boundaries.

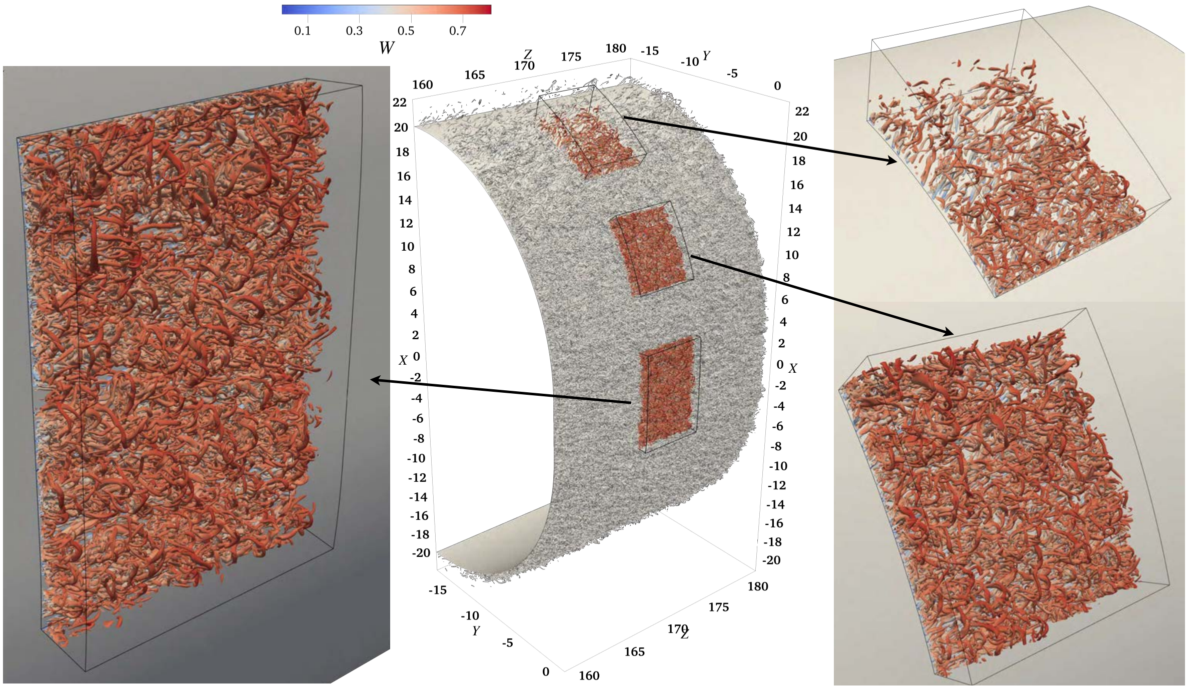

Figure 1: Instantaneous vortical structures visualized by the λ_2 criterion in the swept leading-edge flow. The color indicates the spanwise velocity component. The DNS database is extracted from the fully turbulent downstream region.

The final DNS grid contains $4801 \times 601 \times 2001$ points in (ξ, η, z). The wall-parallel grid spacings satisfy $\Delta\xi^+ < 5$ and $\Delta z^+ < 5$ throughout the entire turbulent boundary layer region. The wall-normal grid provides roughly 50 points across the buffer layer, and the maximum wall-normal spacing normalized by the Kolmogorov scale remains close to unity in the regions of strongest turbulence. Statistical convergence was assessed by comparing independent time windows of Reynolds stresses and dissipation profiles, and by checking the residuals of the Reynolds-stress budgets.

3. Database and diagnostics

3.1 Database organization

$\overline{(\cdot)}$ denotes the time and spanwise average at fixed (ξ, η), and Favre averages are defined by

$$\widetilde{\phi} = \frac{\overline{\rho\phi}}{\overline{\rho}}, \qquad \phi' = \phi - \overline{\phi}, \qquad \phi'' = \phi - \widetilde{\phi}. \tag{3}$$

A DNS field becomes useful for turbulence-model development only when the stored quantities have a clear role in reproducing the case, interpreting the physics, or testing a closure. In the present database, reproducibility is fixed first by the geometry, sweep angle, Mach number, Reynolds number, wall temperature, and shock-layer relation. Once the case is defined, the Favre-averaged velocity, density, temperature, wall shear, skin friction, and heat transfer provide the mean and wall data required by wall models, magnitude-scaling laws, and boundary conditions. These local quantities are not sufficient in a 3D TBL, so the pressure-gradient components, streamline angle, wall-shear angle, acceleration, and curvature are retained at the same stations to record the entire spatial history of the boundary layer. The turbulence data then add Reynolds stresses, turbulent kinetic energy, stress budgets, streak angle, spectra, and turbulent heat fluxes, which show how the stress field, coherent structures, and thermal transport adjust along that history. The last reduction is deliberately diagnostic: the velocity-magnitude log-law residuals, Townsend structure parameter, and stress-anisotropy alignment metric provide direct quantities against which closure assumptions can be tested.

This ordering reflects a practical requirement. A model trained or calibrated only on mean velocity can reproduce a profile while missing the stress direction, production mechanism, or heat-flux coupling. Conversely, a database that includes structural and budget information can distinguish a model that gets the right answer for the wrong reason from one that represents the correct physics.

3.2 Diagnostic quantities for model assessment

The central use of the database is to separate scalar wall scaling from vector and tensor non-equilibrium effects. This separation is made through a set of diagnostic quantities that can be evaluated at each chordwise station. The first diagnostic is the residual of the wall-parallel speed law. With the wall-parallel speed magnitude Q and the Van Driest variables defined later in (19)–(20), the local logarithmic residual is

$$R_Q(\xi, y^+_{VD}) = Q^+_{VD} - \left(\frac{1}{\kappa}\ln y^+_{VD} + B\right), \qquad \kappa = 0.41, \quad B = 5.2. \tag{4}$$

For a station-wise comparison, the residual can be compressed into an overlap-layer error,

$$\epsilon_Q(\xi) = \left[\frac{1}{\Delta \ln y^+}\int_{\mathcal{I}_{log}} R_Q^2(\xi, y^+_{VD})\, d\ln y^+_{VD}\right]^{1/2}, \tag{5}$$

where $\mathcal{I}_{log}$ is the overlap interval used for the station under consideration. In the present paper this residual is used as a diagnostic, not as a claim that a universal 3D log law has been established for all pressure-gradient histories.

The second group of diagnostics measures directional behavior. The angle between the wall-shear vector and the local wall-parallel mean velocity at a wall-normal position η is

$$\cos\Delta\theta_{\tau u}(\eta) = \frac{\boldsymbol{\tau}_{w,\parallel}\cdot\widetilde{\boldsymbol{u}}_\parallel(\eta)}{|\boldsymbol{\tau}_{w,\parallel}|\,|\widetilde{\boldsymbol{u}}_\parallel(\eta)|}. \tag{6}$$

For the near-wall streaks, the two angles used in the results section are

$$\Delta\theta_{w-st} = \theta_{w,s} - \theta_{s,s}, \qquad \Delta\theta_{st-e} = \theta_{s,s} - \theta_s. \tag{7}$$

These quantities test whether the wall shear, coherent structures, and external streamline can be described by a single local direction. They are deliberately separate from the scalar residual in (4), because a model can match the wall-speed magnitude while predicting a wrong orientation.

The Reynolds-stress diagnostics use the Favre stress tensor

$$R_{ij} = \frac{\overline{\rho\, u_i'' u_j''}}{\overline{\rho}}, \qquad k = \frac{1}{2}R_{ii}, \qquad b_{ij} = \frac{R_{ij}}{2k} - \frac{1}{3}\delta_{ij}. \tag{8}$$

The turbulent-kinetic-energy production is

$$P_k = -\overline{\rho}\, R_{ij}\frac{\partial \widetilde{u}_i}{\partial x_j}. \tag{9}$$

In a wall-bounded local streamline frame, the dominant wall-normal shear contributions are

$$P_{k,\eta} \approx -\overline{\rho}\left(R_{s\eta}\frac{\partial \widetilde{u}_s}{\partial \eta} + R_{c\eta}\frac{\partial \widetilde{u}_c}{\partial \eta}\right), \tag{10}$$

with additional terms retained in the full budget. The comparison between (9) and the dissipation rate

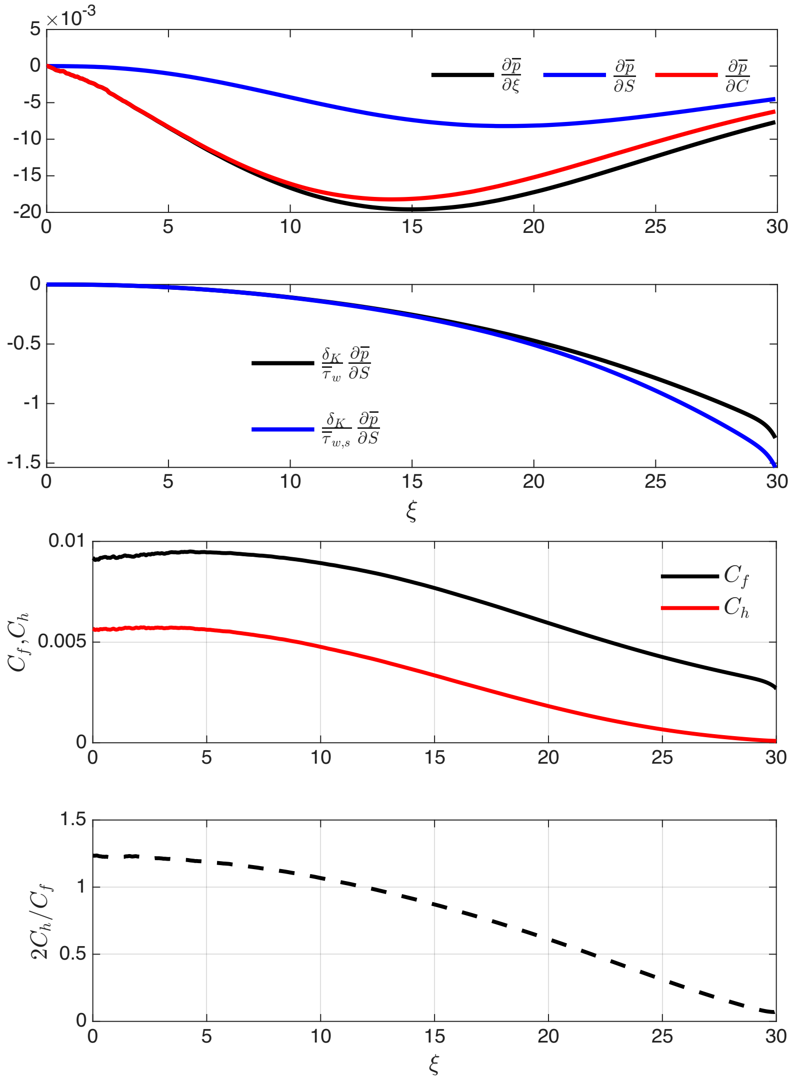

Figure 2: Pressure-gradient history and wall quantities along the chordwise direction. Upper panels: pressure-gradient components and streamwise Rotta–Clauser parameters. Lower panels: skin friction, heat-transfer coefficient, and Reynolds analogy factor.

provides the relaminarization diagnostic used in Figure 7.

The thermal diagnostics are defined in the same local frame. The turbulent heat-flux vector is

$$H_i = \overline{\rho\, u_i'' T''}, \qquad i = s, \eta, c, \tag{11}$$

and the corresponding velocity-temperature correlation coefficient is

$$R_{u_i T} = -\frac{\overline{\rho\, u_i'' T''}}{\left(\overline{\rho\, u_i'' u_i''}\right)^{1/2} \left(\overline{\rho\, T'' T''}\right)^{1/2}}. \tag{12}$$

Together, (5)–(12) define a model-assessment protocol: a successful 3D TBL closure should not only reproduce scalar wall quantities, but also the wall-shear direction, stress-anisotropy orientation, production level, and heat-flux alignment.

3.3 Wall scaling and pressure-gradient history

The inner coordinate uses the magnitude of the total wall-shear vector,

$$u_\tau = \sqrt{\tau_w/\rho_w}, \qquad \tau_w = \left(\tau_{w,s}^2 + \tau_{w,c}^2\right)^{1/2}, \qquad h^+ = \frac{\rho_w u_\tau \eta}{\mu_w}. \tag{13}$$

The wall-shear vector and wall-shear angle in the local streamline frame are

$$\boldsymbol{\tau}_{w,\parallel} = \tau_{w,s}\boldsymbol{e}_S + \tau_{w,c}\boldsymbol{e}_C, \qquad \theta_{w,s} = \tan^{-1}\left(\frac{\tau_{w,c}}{\tau_{w,s}}\right). \tag{14}$$

In a 3D TBL this total shear is not sufficient to describe the turbulence cycle. The streamwise wall-shear component, the crossflow wall-shear component, and the pressure-gradient vector must be retained separately because the crossflow component can be strongly pressure-gradient driven. This distinction is central to model development: u_τ can scale the magnitude of the wall-parallel mean velocity, but it cannot determine the direction of the velocity vector, the wall-shear vector, or the Reynolds-stress anisotropy.

The wall-parallel pressure-gradient history is decomposed in the same frame,

$$\nabla_\parallel \overline{p} = \left(\frac{\partial \overline{p}}{\partial S}\right)\boldsymbol{e}_S + \left(\frac{\partial \overline{p}}{\partial C}\right)\boldsymbol{e}_C. \tag{15}$$

Figure 2 shows that the downstream boundary layer is exposed to a strong favorable pressure gradient while the wall heat transfer and Reynolds analogy factor decline. These quantities are stored as part of the database because they document the pressure-gradient and wall-transfer history that a local mean profile alone cannot reconstruct.

3.4 Near-wall streak orientation

The near-wall streak angle is a compact structural observable for model assessment. It measures how the organized near-wall motions are oriented relative to the external streamline and the wall-shear vector. The procedure used here has four steps.

First, a wall-parallel plane is selected in the buffer layer, near $h^+ \approx 15$, where the near-wall streaks and turbulence production are most visible. At each chordwise station ξ_0, the spanwise velocity fluctuation is used as the marker variable, $\phi = w'$. This choice follows the instantaneous visualizations: as the flow turns downstream, the skewed near-wall structures appear clearly in the spanwise-velocity fluctuation field.

Second, a two-point correlation map is formed on that wall-parallel plane. For a general fluctuation ϕ,

$$C_\phi(\xi_0, \eta_0; \Delta\xi, \Delta z) = \frac{\langle \phi(\xi_0 + \Delta\xi, \eta_0, z + \Delta z, t)\phi(\xi_0, \eta_0, z, t)\rangle_{z,t}}{\left[\left\langle \phi^2(\xi_0 + \Delta\xi, \eta_0, z + \Delta z, t)\right\rangle_{z,t} \left\langle \phi^2(\xi_0, \eta_0, z, t)\right\rangle_{z,t}\right]^{1/2}}, \tag{16}$$

where $\langle\cdot\rangle_{z,t}$ denotes averaging over the homogeneous spanwise direction and time. The correlation map $C_\phi(\Delta\xi, \Delta z)$ gives the local footprint of the streaks around the reference point. If a fixed contour level is chosen, for example $C_\phi = 0.7$, the contour can be fitted by an ellipse and the major axis gives a streak orientation. This construction is intuitive, but the fitted angle can depend weakly on the selected contour level.

Third, to remove this arbitrary contour choice, the orientation is defined from the local curvature of the correlation peak. Near $\Delta\xi = \Delta z = 0$, the two-point correlation is approximated as

$$C_\phi(\Delta\xi, \Delta z) \approx 1 + \frac{1}{2}\begin{bmatrix}\Delta\xi & \Delta z\end{bmatrix} \boldsymbol{H} \begin{bmatrix}\Delta\xi \\ \Delta z\end{bmatrix}, \qquad \boldsymbol{H} = \begin{bmatrix} \frac{\partial^2 C_\phi}{\partial \Delta\xi^2} & \frac{\partial^2 C_\phi}{\partial \Delta\xi \partial \Delta z} \\ \frac{\partial^2 C_\phi}{\partial \Delta z \partial \Delta\xi} & \frac{\partial^2 C_\phi}{\partial \Delta z^2} \end{bmatrix}. \tag{17}$$

The eigenvectors of $\boldsymbol{H}$ define the axes of the local correlation ellipse. Equivalently, writing the entries of $\boldsymbol{H}$ as $C_{\xi\xi}$, $C_{\xi z}$, and C_{zz}, the principal-axis angle satisfies

$$\tan 2\theta_{s,s} = \frac{2C_{\xi z}}{C_{\xi\xi} - C_{zz}}. \tag{18}$$

The angle $\theta_{s,s}$ is then reported using the same angular convention as the external streamline angle θ_s and the wall-shear angle $\theta_{w,s}$.

Finally, this Hessian-based estimator is applied at each stored chordwise station. It is local, threshold-free, and storage-efficient. It avoids choosing an arbitrary correlation-contour level and agrees with conventional ellipse fitting within approximately one degree for representative DNS samples. The resulting sequence of $\theta_{s,s}(\xi)$ is used in Section 4 to quantify the structural lag between the external streamline, near-wall streaks, and wall-shear vector.

4. Results and discussion

The analysis proceeds from the mean-flow development to the turbulence statistics. We first describe the wall quantities and pressure-gradient history. We then test whether a scalar wall-speed scaling remains useful. The following sections examine the quantities not determined by that scalar law: orientation of near-wall structures, Reynolds-stress production, spectral content, and heat transfer. The present DNS is not used only as a collection of profiles; it is used to trace how a realistic three-dimensional pressure-gradient and streamline history appears in different modeling variables. The first part of the results identifies what remains partly compatible with classical wall scaling. The later parts identify the vector, tensor, budget, and spectral quantities that do not follow from that scalar constraint.

4.1 Mean-flow development

The swept leading edge provides a physically meaningful path from one turbulence state to another. Near the attachment line, the boundary layer is close to a quasi-two-dimensional attachment-line turbulent boundary layer. Downstream, the same turbulence is convected through increasing crossflow, strong favorable pressure gradient, and geometric curvature. Figure 3 shows that the chordwise velocity accelerates and develops a velocity overshoot, while the crossflow angle grows continuously to approximately 35° by the chordwise exit.

This route is important for modeling because the downstream boundary layer cannot be interpreted as a locally rotated two-dimensional boundary layer. Its state depends on how long the turbulence has been exposed to acceleration and crossflow. The wall-transfer quantities reflect this history: skin friction and heat transfer decrease downstream after a weak initial rise, and the Reynolds analogy factor is not constant. A local-equilibrium model could match one station only by losing predictive consistency at another station.

4.2 Wall-parallel speed scaling

The wall-similarity idea for 3D TBLs has a long experimental history: the near-wall profiles are not universal component by component, but suitable resultant velocity and resultant friction-velocity scalings can retain part of the classical inner structure [3, 4, 5]. We use this idea as a wall-model diagnostic for

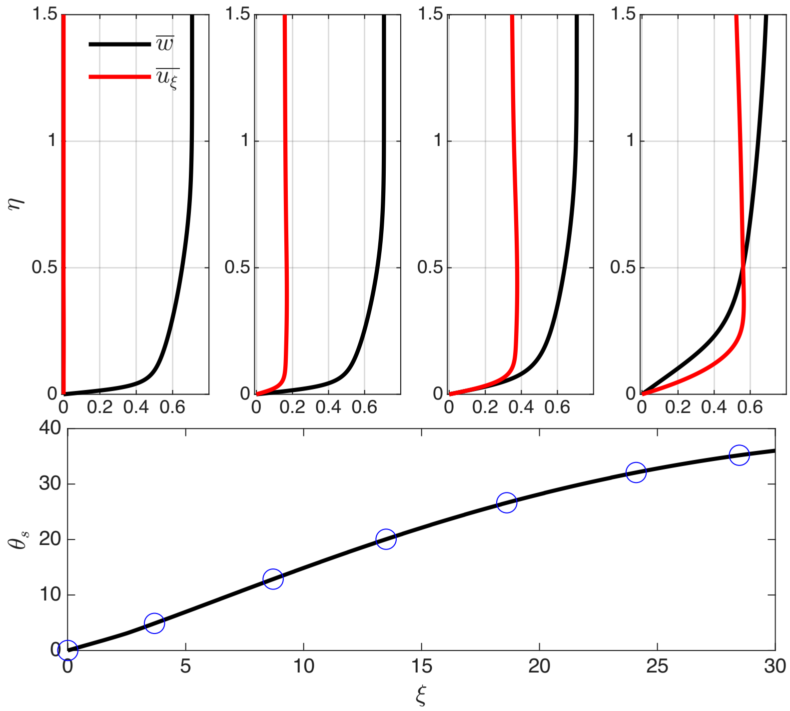

Figure 3: Mean chordwise and spanwise velocity profiles and the chordwise evolution of the external crossflow angle. The upper panels show velocity profiles at representative stations, and the lower panel shows the external crossflow angle. The database captures a continuous transition from attachment-line turbulence to a strongly skewed 3D TBL.

the present compressible DNS. Let

$$Q = |\widetilde{\boldsymbol{u}}_{\parallel}| = \left(\widetilde{u}_s^2 + \widetilde{u}_c^2\right)^{1/2}, \qquad Q^+ = Q/u_\tau, \tag{19}$$

where $\widetilde{\boldsymbol{u}}_{\parallel}$ is the wall-parallel mean velocity vector. For the compressible present case, the Van Driest transformed wall-parallel speed is evaluated as

$$Q^+_{VD} = \int_0^{Q^+} \left(\frac{\overline{\rho}}{\rho_w}\right)^{1/2} dQ^+, \qquad y^+_{VD} = \int_0^{h^+} \left(\frac{\overline{\rho}}{\rho_w}\right)^{1/2} dh^+. \tag{20}$$

Both integrals are evaluated along each wall-normal profile at a fixed chordwise station. The density weighting therefore corrects the local compressible inner coordinate without mixing different streamwise histories. The corresponding magnitude law is written

$$Q^+_{VD} \approx y^+_{VD} \quad (y^+_{VD} \lesssim 5), \qquad Q^+_{VD} \approx \frac{1}{\kappa} \ln y^+_{VD} + B \quad \text{(overlap layer)}, \tag{21}$$

where $\kappa = 0.41$ and $B = 5.2$ are the classical constants.

Figure 4 compares the present hypersonic swept-leading-edge DNS with the shear-driven 3D TBL DNS of Abe [9]. The agreement is not used here to claim complete universality, especially outside the overlap layer where the present boundary layer is accelerated and relaminarizing. Rather, it gives a limited but useful wall constraint: the near-wall speed magnitude can be checked against a classical law, while the orientation of the wall-parallel velocity, the wall-shear vector, and the Reynolds-stress tensor remains a separate three-dimensional modeling problem. The next subsection therefore turns from the scalar magnitude to the orientation of the near-wall structures.

This result narrows the modeling problem. It suggests that a scalar wall function based on Q and u_τ may

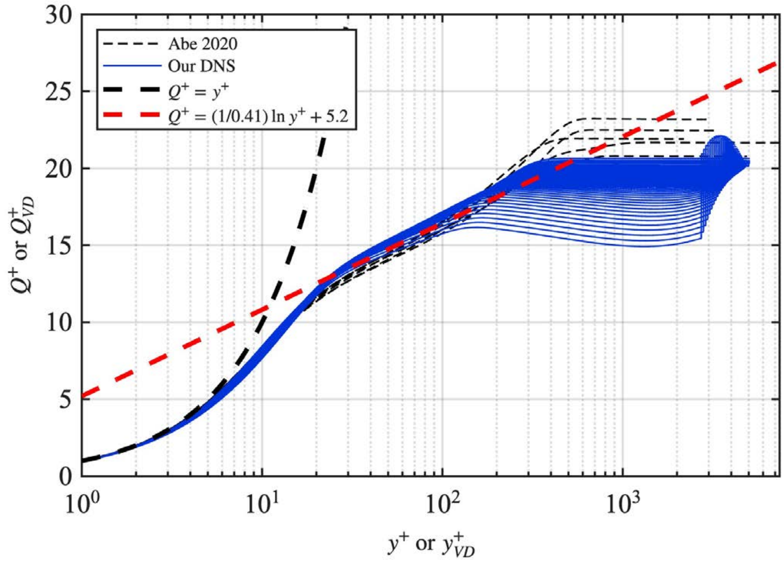

Figure 4: Wall-parallel speed scaling in 3D TBLs. In both the present DNS and the shear-driven 3D TBL DNS of Abe [9], Q^+_{VD} approximately recovers the viscous scaling near the wall and the classical logarithmic behavior over the overlap range, even though the velocity components and wall-shear direction are strongly three-dimensional.

remain a useful first constraint for the mean-speed magnitude, but it also shows what such a wall function cannot determine. It cannot specify whether the wall shear is aligned with the external streamline, whether the streaks have adjusted to the local pressure-gradient direction, or whether the Reynolds-stress tensor has the correct orientation. The central question therefore shifts from whether any wall scaling survives to how the remaining vector and tensor information should be represented.

4.3 Structural lag of near-wall streaks

The clearest structural marker of non-equilibrium is the lag between the near-wall streaks, wall shear, and external streamline. Figure 5 shows the hierarchy

$$\theta_{w,s} > \theta_{s,s} > \theta_s, \tag{22}$$

where $\theta_{w,s}$ is the wall-shear angle, $\theta_{s,s}$ is the streak angle, and θ_s is the external-streamline angle. Near the chordwise exit, the wall shear rotates to nearly 70°, but the streaks remain much closer to the external streamline. The structures therefore preserve upstream memory instead of instantaneously aligning with the local wall-stress vector.

For turbulence modeling, this observable is valuable because it probes physics that mean profiles alone cannot reveal. A closure may predict a plausible wall-shear magnitude while placing the modeled anisotropy tensor in the wrong direction. A model-ready 3D TBL database should therefore include orientation metrics, not only scalar skin friction and heat transfer.

The angle hierarchy also gives a useful interpretation of the downstream flow. The wall shear responds most directly to the local crossflow pressure gradient, the external streamline reflects the outer inviscid turning, and the streak angle lies between them. The intermediate position of $\theta_{s,s}$ is consistent with a finite adjustment time of near-wall structures. This is the first point at which the present case differs qualitatively from a locally rotated two-dimensional boundary layer: rotating the coordinate system can align one vector, but it cannot remove the lag among the external flow, wall stress, and turbulence structure.

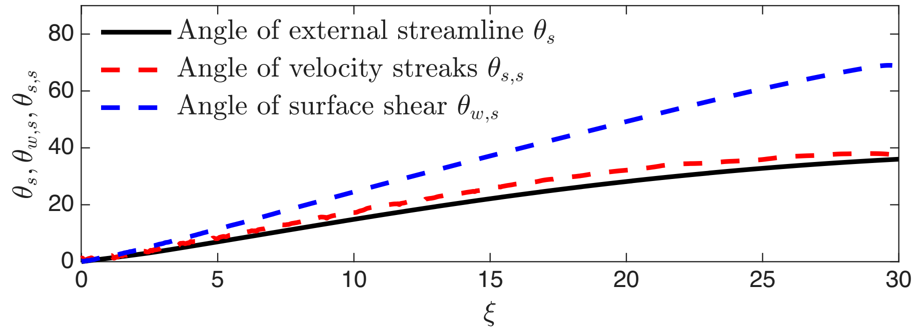

Figure 5: Chordwise evolution of the external streamline angle, near-wall streak angle, and wall-shear angle. The persistent hierarchy $\theta_{w,s} > \theta_{s,s} > \theta_s$ turns structural lag into a quantitative database target for model assessment.

4.4 Reynolds-stress depletion and relaminarization

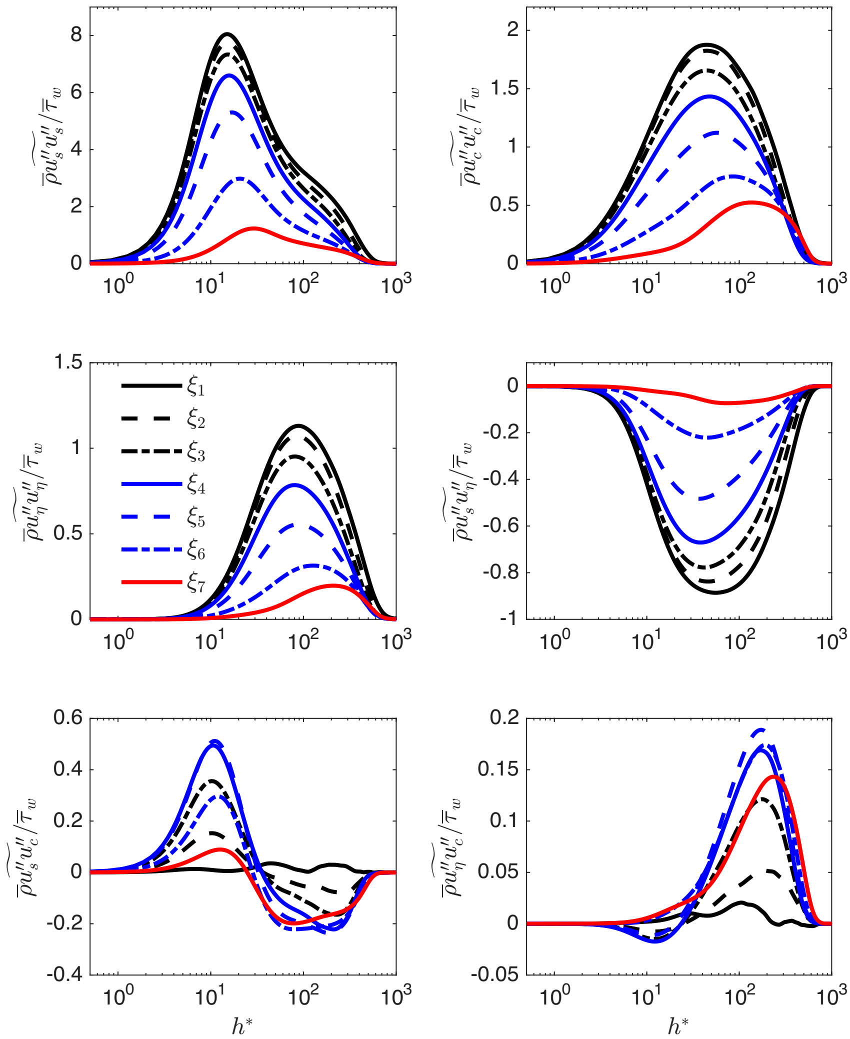

Figure 6: Reynolds-stress components at seven chordwise stations in the local streamline coordinate system. Stress depletion proceeds downstream and the primary shear stress nearly vanishes near the chordwise exit.

The structural lag is accompanied by a strong reduction of turbulence stresses. Figure 6 shows Reynolds-stress components in the local (S, η, C) frame, by using the semi-local scaling h^*. The streamwise

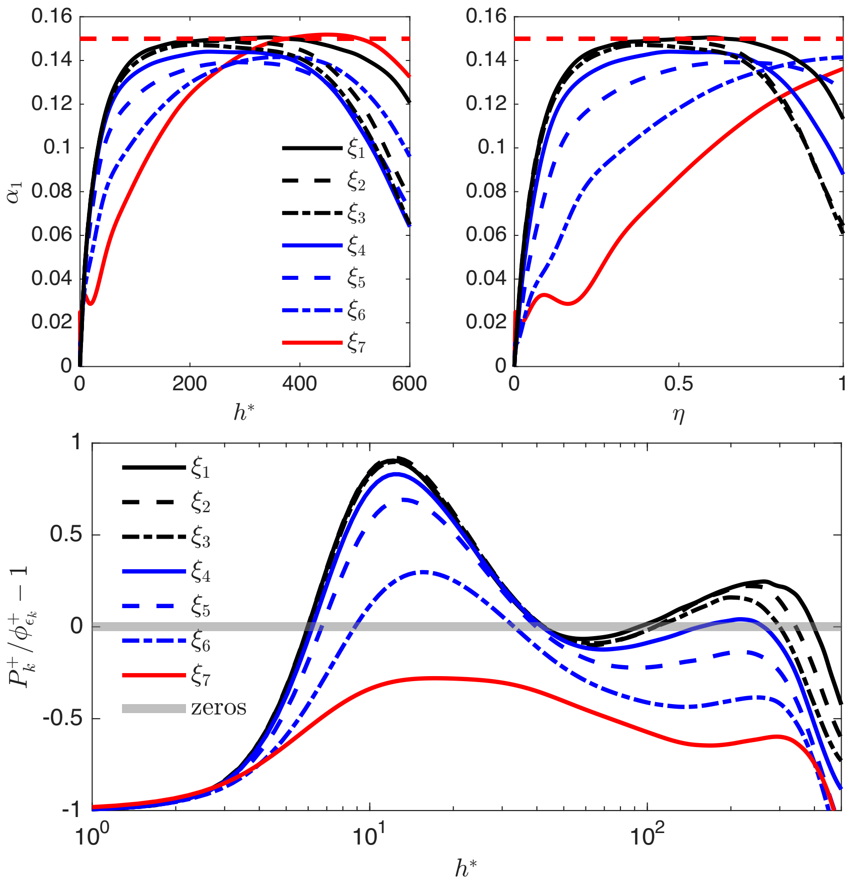

Figure 7: Townsend structure parameter and turbulent-kinetic-energy production–dissipation balance. Upper panels: surface-normal profiles of α_1. Lower panel: the ratio $P_k^+/\phi_{\epsilon_k}^+ - 1$. The downstream collapse of α_1 and the production deficit show that the turbulence regeneration cycle is no longer locally self-sustaining.

normal stress and the primary shear stress decrease monotonically downstream; the primary shear stress nearly vanishes near the chordwise exit even though the mean boundary layer is highly three-dimensional. Crossflow-related stresses initially grow as crossflow shear develops, but then collapse as acceleration dominates the turbulence-production mechanism.

The Townsend structure parameter gives a compact measure of how efficiently velocity fluctuations generate shear stress,

$$\alpha_1 = \frac{\sqrt{\overline{u_s''u_\eta''}^2 + \overline{u_\eta''u_c''}^2}}{2k}, \qquad k = \frac{1}{2}\left(\overline{u_s''u_s''} + \overline{u_\eta''u_\eta''} + \overline{u_c''u_c''}\right). \tag{23}$$

As shown in Figure 7, α_1 falls below the equilibrium value of about 0.15 over a large part of the downstream boundary layer. This is not simply a decay of turbulent kinetic energy. It is a loss of structural efficiency: the remaining fluctuations no longer generate the shear stress needed to sustain equilibrium turbulence.

The turbulent-kinetic-energy budget confirms the same mechanism. Downstream, the production-to-dissipation ratio collapses, and at the chordwise exit production is smaller than dissipation over nearly the entire boundary layer. The flow is therefore undergoing continuous spatial relaminarization. The term “relaminarization” here does not mean that all fluctuations disappear. It means that the local turbulence regeneration cycle is no longer self-sustaining under the imposed acceleration and three-dimensional strain history.

This distinction is important because crossflow alone would not necessarily imply relaminarization. A three-dimensional shear can create additional stress components and can increase selected crossflow-related fluctuations. In the present case, however, the acceleration reduces the primary stress-production pathway faster than the crossflow terms can compensate. The observed collapse of α_1 and P_k/ϕ_{ϵ_k} therefore links the geometry-driven acceleration to a specific failure of local-equilibrium assumptions: the remaining turbulent kinetic energy is not organized efficiently into shear stress.

4.5 Spectra and turbulent heat transfer

Spectral analysis shows that relaminarization is scale selective. Figure 8 presents premultiplied spanwise spectra of velocity and temperature fluctuations at representative chordwise stations. At the attachment line, energy is concentrated at low spanwise wavenumber because the coherent structures are elongated along the attachment-line direction. Downstream, the energetic peak shifts to higher wavenumber as the near-wall streaks become oblique. Near the chordwise exit, the low-wavenumber energy is strongly reduced while a near-wall streak scale remains visible.

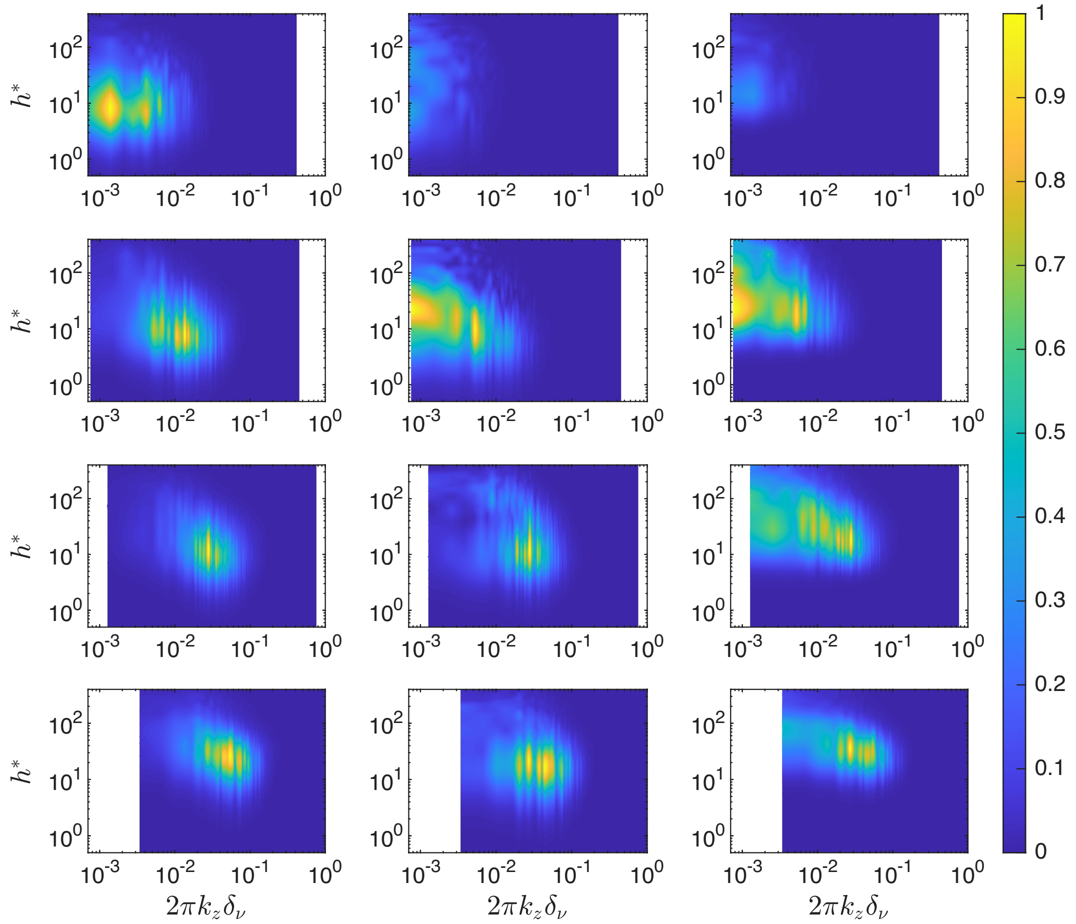

Figure 8: Premultiplied spanwise spectra of velocity and temperature fluctuations. Large-scale energy is suppressed downstream, while skewed near-wall streaks survive and remain thermally correlated.

The temperature spectra remain topologically similar to the velocity spectra, showing that the thermal field stays locked to the surviving momentum streaks. In the local streamline coordinate system, the streamwise turbulent heat flux follows the streamwise momentum fluctuation, whereas wall-normal and crossflow heat fluxes are strongly reduced downstream. For high-speed turbulence modeling, this is a central constraint: momentum and thermal closures cannot be tuned independently when the surviving structures transport both fields.

The spectral evidence completes the sequence from wall quantities to turbulence structure. The wall-speed magnitude remains partly constrained by inner scaling, the streaks retain a directional memory, and the stress budget shows that the turbulence is losing production efficiency. The spectra then show how this loss occurs across scales: large-scale motions are preferentially suppressed, while a smaller near-wall streak scale persists. This scale selectivity explains why the downstream state should not be described simply as either fully turbulent or laminar; it is a non-equilibrium state in which selected structures survive but no longer sustain the usual stress-production cycle.

5. Implications for turbulence modeling

5.1 Modeling requirements

The preceding results separate four aspects that are often coupled in simpler wall-bounded flows: the magnitude of the wall-parallel mean velocity, the direction of the wall shear and near-wall structures, the ability of the Reynolds stresses to produce turbulent kinetic energy, and the thermal transport associated with the surviving streaks. A direct modeling implication is that a model can satisfy one of these constraints while failing another; for example, a wall treatment may reproduce a plausible friction scale while still predicting the wrong stress orientation or production level.

For turbulence models intended for realistic 3D TBLs, the DNS therefore suggests four requirements. First, wall models should separate magnitude from direction. The wall-parallel mean-speed magnitude can be constrained by the 3D law of the wall in (21), but the wall-shear direction, velocity-vector direction, pressure-gradient direction, and structural orientation still require vectorial or history-aware modeling. Second, Reynolds-stress closures must represent stress–strain misalignment and pressure–strain redistribution under rapid three-dimensional distortion. Third, dissipation and length-scale models must respond to favorable-pressure-gradient relaminarization and should not assume local production–dissipation balance. Fourth, heat-flux closures must account for thermal-momentum lock-in of surviving streaks in compressible flow.

These requirements favor wall treatments that combine a simple magnitude constraint with second-moment closures or nonlinear constitutive relations for direction and anisotropy. Differential Reynolds-stress models provide a natural framework for pressure–strain redistribution and history effects, but their closure terms must be constrained by data from realistic 3D TBLs [14, 15, 16]. Nonlinear eddy-viscosity and explicit algebraic stress models can improve stress orientation when strain–rotation and higher-order tensor products are included in a controlled form [17, 18]. Wall-modeled LES and data-assisted models can also benefit from the same database if the training targets include wall-speed magnitude, wall-vector orientation, stress orientation, spectra, and heat fluxes rather than mean velocity only.

5.2 Stress-anisotropy alignment

As a first model-assessment metric, we compare the stress-orientation prediction of the conventional linear eddy-viscosity tensor with one nonlinear eddy-viscosity form obtained from the present DNS data. This comparison follows the companion analysis and is included here only to show how the database can be used to test tensor orientation. The nonlinear form should not be read as a universal closure.

The mean strain-rate and rotation-rate tensors are

$$S_{ij} = \frac{1}{2}\left(\frac{\partial \widetilde{u}_i}{\partial x_j} + \frac{\partial \widetilde{u}_j}{\partial x_i}\right), \qquad \Omega_{ij} = \frac{1}{2}\left(\frac{\partial \widetilde{u}_i}{\partial x_j} - \frac{\partial \widetilde{u}_j}{\partial x_i}\right). \tag{24}$$

We also use the gradient magnitude

$$\|\nabla \boldsymbol{U}\| = \left[\mathrm{tr}\left(\boldsymbol{S}^2\right) - \mathrm{tr}\left(\boldsymbol{\Omega}^2\right)\right]^{1/2}. \tag{25}$$

After removing the scalar eddy-viscosity magnitude, the major tensorial part of the linear eddy-viscosity model can be written as

$$T_{ij,L} = S_{ij} - \frac{1}{3}S_{kk}\delta_{ij}. \tag{26}$$

The nonlinear tensor used in the comparison is

$$\begin{aligned} T_{ij,N} =& S_{ij} - \frac{1}{3}S_{kk}\delta_{ij} \\ & - \frac{C_1}{\|\nabla \boldsymbol{U}\|}\left(S_{ik}\Omega_{kj} + S_{jk}\Omega_{ki}\right) - \frac{C_2}{\|\nabla \boldsymbol{U}\|}\left(S_{ik}S_{jk} - \frac{1}{3}S_{mn}S_{mn}\delta_{ij}\right) \\ & - \frac{C_3}{\|\nabla \boldsymbol{U}\|}\left(\Omega_{ik}\Omega_{kj} - \frac{1}{3}\delta_{ij}\mathrm{tr}\left(\boldsymbol{\Omega}^2\right)\right) - \frac{C_4}{\|\nabla \boldsymbol{U}\|}\left(\Omega_{im}S_{mn}S_{nj} + \Omega_{jm}S_{mn}S_{ni}\right). \end{aligned} \tag{27}$$

For illustration, the coefficients are set to

$$C_1 = -0.9, \qquad C_2 = 0.25, \qquad C_3 = 0.25, \qquad C_4 = 0.1. \tag{28}$$

These coefficients are empirical and are not claimed to be optimal or universal. They are used only to demonstrate whether a nonlinear constitutive form can reduce the tensor-orientation error that is inherent in the linear Boussinesq assumption.

The comparison uses the tensor direction cosine

$$\sigma_{lag} = -\frac{T_{ij}b_{ij}^{DNS}}{\left(T_{ij}T_{ij}\right)^{1/2}\left(b_{ij}^{DNS}b_{ij}^{DNS}\right)^{1/2}}, \tag{29}$$

where b_{ij}^{DNS} is the Reynolds-stress anisotropy tensor defined in (8), and T_{ij} denotes either $T_{ij,L}$ or $T_{ij,N}$. The minus sign follows the eddy-viscosity convention. A value close to unity indicates that the modeled tensor is aligned with the DNS anisotropy tensor, independent of the stress magnitude error.

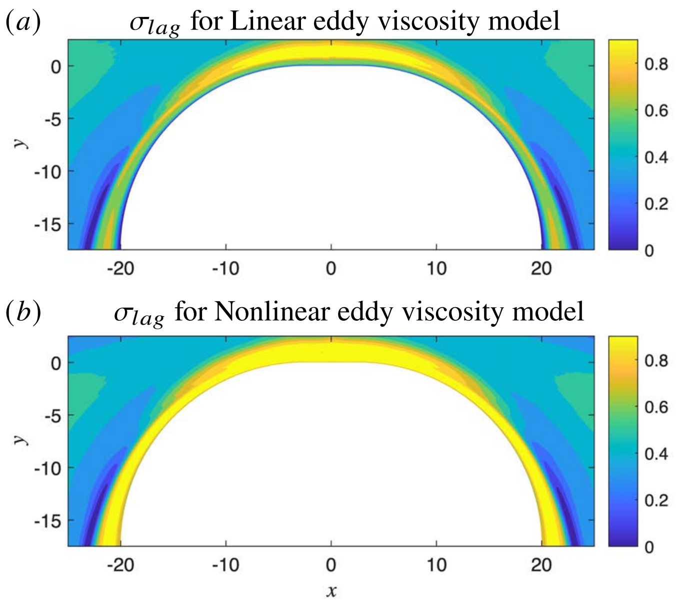

Figure 9: Direction cosine σ_{lag} between modeled and DNS Reynolds-stress anisotropy tensors. The upper panel uses the linear eddy-viscosity tensor $T_{ij,L}$, and the lower panel uses the empirical nonlinear eddy-viscosity tensor $T_{ij,N}$ in (27). The nonlinear form improves the predicted stress orientation for the present 3D TBL.

Figure 9 shows the direction cosine σ_{lag} between modeled and DNS Reynolds-stress anisotropy tensors. The linear model deteriorates downstream as the flow becomes more skewed and non-equilibrium. With the empirical coefficients in (28), the nonlinear form maintains σ_{lag} near 0.9 over much of the boundary layer. This result should not be read as a complete turbulence model or as a universal calibration. The spatial memory, stress-peak migration, production deficit, and thermal coupling still require transport equations, calibrated relaxation terms, or history-sensitive closures. It does show, however, how a DNS database can move beyond qualitative flow physics and provide direct tests for stress-orientation errors.

5.3 Scope of the present assessment

The present conference paper is intentionally limited in three respects. First, the wall-parallel speed law is tested for the present swept-leading-edge DNS and compared with the shear-driven 3D TBL DNS of Abe [9]. This supports the use of Q^+_{VD} as a useful diagnostic, but it does not establish a universal law for arbitrary pressure-gradient, Mach-number, or wall-temperature histories. The residuals in (4) and (5) are included for that reason: future cases can test where the scaling holds and where it fails.

Second, the anisotropy comparison is a limited stress-orientation test rather than a complete turbulence-model validation. The direction cosine σ_{lag} removes the magnitude of the modeled tensor and focuses on orientation. This is useful because tensor direction is a major difficulty in 3D TBLs, but the nonlinear form used here is only an empirical example from the present data. A deployable closure must also predict stress magnitude, redistribution, dissipation, and wall heat flux, and its coefficients must be tested beyond this configuration. Third, the present DNS is one realistic configuration, not a parametric database. Its value is that it provides a resolved case in which pressure-gradient history, wall quantities, and tensor statistics are available together; broader generality requires a controlled set of related cases.

5.4 Extension of the database

The present case should be viewed as one member of a broader database strategy. A database family for 3D TBL modeling should vary sweep angle, Mach number, wall temperature, pressure-gradient strength, leading-edge radius, and roughness-induced transition history. Each member should document the same categories of information: reproducible configuration, mean and wall quantities, pressure-gradient and streamline history, turbulence statistics, budget terms, spectra, and model-assessment metrics. Such a family would allow model developers to separate robust mechanisms from case-specific behavior and to test whether a closure extrapolates across realistic three-dimensional histories.

For practical use, each streamwise station can be indexed by a station-descriptor vector

$$\boldsymbol{s}(\xi) = \left[M_e,\ Re_\tau,\ T_w/T_e,\ \theta_s,\ \theta_{w,s},\ \frac{\partial \overline{p}}{\partial S},\ \frac{\partial \overline{p}}{\partial C},\ C_f,\ C_h \right]_\xi , \tag{30}$$

and a reduced diagnostic vector

$$\boldsymbol{d}(\xi) = \left[\epsilon_Q,\ \Delta\theta_{w-st},\ \alpha_1,\ P_k/\phi_{\epsilon_k},\ \sigma_{lag},\ H_s,\ H_\eta,\ H_c \right]_\xi . \tag{31}$$

The pair $\{\boldsymbol{s}(\xi), \boldsymbol{d}(\xi)\}$ gives a compact station-by-station index of the local flow state and selected diagnostic measures. It should not be interpreted as a causal input–output representation, and it is not a replacement for the full DNS fields. Its purpose is practical: it allows model developers to compare different 3D TBL cases without first reducing each database in a different way.

Experiments remain essential for anchoring geometry, transition, and integral quantities. DNS complements them by supplying the tensor, budget, and spectral information that is difficult to obtain in high-speed 3D configurations. A controlled set of such cases would make it possible to test which wall-scaling, stress-orientation, heat-flux, and history effects remain consistent across realistic three-dimensional boundary layers.

6. Conclusions

A DNS of a Mach-6 swept leading-edge turbulent boundary layer has been presented as a prototype model-ready database for realistic high-speed 3D TBL modeling. The flow evolves naturally from a quasi-two-dimensional attachment-line turbulent boundary layer into a strongly skewed, favorable-pressure-gradient-dominated downstream boundary layer. The final DNS contains $4801 \times 601 \times 2001$ points, resolves the relevant near-wall and small-scale motions, and stores not only mean fields but also model-relevant structural, budget, spectral, wall-vector, wall-transfer, and closure-error diagnostics.

The main physical findings are as follows. First, the wall-parallel mean-speed magnitude approximately recovers a classical inner-layer structure: Q^+_{VD} follows viscous scaling near the wall and logarithmic behavior over the overlap range. Second, this magnitude law does not remove three-dimensional non-equilibrium; near-wall streaks exhibit a persistent structural lag, with $\theta_{w,s} > \theta_{s,s} > \theta_s$. Third, favorable-pressure-gradient acceleration ultimately dominates crossflow-driven production, causing Reynolds-stress depletion, collapse of the Townsend structure parameter, and a turbulent-kinetic-energy production deficit. Fourth, the relaminarization is scale selective. Large-scale motions are suppressed, while skewed near-wall streaks survive and remain thermally locked to the temperature field. Finally, the DNS exposes specific closure failures of component-wise wall assumptions and linear eddy-viscosity models, while showing that an empirical nonlinear eddy-viscosity form can improve stress-orientation prediction for this case.

For realistic 3D TBLs, the database variables needed for model development are not only velocity and temperature profiles, but also wall-speed magnitude, pressure-gradient and streamline history, stress anisotropy, structure orientation, heat-flux coupling, and model-error metrics. Building such datasets across a controlled set of configurations is a practical route toward more predictive turbulence models for three-dimensional high-speed aerodynamic flows.

Acknowledgements

This work received support from the NSFC Grants 12388101, U2541235, 12202242 and 12172195. The authors acknowledge the computational resources provided by the Yancheng Supercomputing Center under project number 20231001 and Yancheng MetaStone Tech. Co. for additional computational support. Useful discussions with Professor Michael Leschziner of Imperial College London and Dr Jian Liu of China Aerodynamics Research and Development Center are gratefully acknowledged.

References

[1] H. Schlichting and K. Gersten. *Boundary-Layer Theory*. Springer-Verlag Berlin Heidelberg, 9 edition, 2017.

[2] W. J. Devenport and K. T. Lowe. Equilibrium and non-equilibrium turbulent boundary layers. *Progress in Aerospace Sciences*, 131:100807, 2022.

[3] T. S. Prahlad. Wall similarity in three-dimensional turbulent boundary layers. *AIAA Journal*, 6(9):1772–1774, 1968.

[4] F. J. Pierce and B. B. Zimmerman. Wall shear stress inference from two- and three-dimensional turbulent boundary layer velocity profiles. *Journal of Fluids Engineering*, 95(1):61–67, 1973.

[5] K. S. Hebbar and W. L. Melnik. Wall region of a relaxing three-dimensional incompressible turbulent boundary layer. *Journal of Fluid Mechanics*, 85(1):33–56, 1978.

[6] P. R. Spalart. Theoretical and numerical study of a three-dimensional turbulent boundary layer. *Journal of Fluid Mechanics*, 205:319–340, 1989.

[7] P. Moin, T.-H. Shih, D. Driver, and N. N. Mansour. Direct numerical simulation of a three-dimensional turbulent boundary layer. *Physics of Fluids A*, 2(10):1846–1853, 1990.

[8] A. Lozano-Durán, M. G. Giometto, G. I. Park, and P. Moin. Non-equilibrium three-dimensional

boundary layers at moderate Reynolds numbers. *Journal of Fluid Mechanics*, 883:A20, 2020.

[9] H. Abe. Direct numerical simulation of a non-equilibrium three-dimensional turbulent boundary layer over a flat plate. *Journal of Fluid Mechanics*, 902:A20, 2020.

[10] S. R. Gomez. Direct numerical simulations of supersonic three-dimensional turbulent boundary layers. *Journal of Fluid Mechanics*, 1022:A17, 2025.

[11] Y. Xi, B. Yan, G. Yang, X. Sha, D. Zhu, and S. Fu. Numerical simulations of attachment-line boundary layer in hypersonic flow. Part 1. roughness-induced subcritical transitions. *Journal of Fluid Mechanics*, 1009:A63, 2025.

[12] X. Li, D. Fu, and Y. Ma. Direct numerical simulation of hypersonic boundary layer transition over a blunt cone. *AIAA Journal*, 46(11):2899–2913, 2008.

[13] G. Dang, S. Liu, T. Guo, J. Duan, and X. Li. Direct numerical simulation of compressible turbulence accelerated by graphics processing unit: An open-source high accuracy accelerated computational fluid dynamic software. *Physics of Fluids*, 34(12):126106, 2022.

[14] K. Hanjalić and B. E. Launder. Reassessment of modeling turbulence via Reynolds averaging: A review of second-moment transport strategy. *Physics of Fluids*, 33(9):091302, 2021.

[15] T. J. Craft and B. E. Launder. Principles and performance of TCL-based second-moment closures. *Flow, Turbulence and Combustion*, 66(4):355–372, 2001.

[16] S. Jakirlić and K. Hanjalić. A new approach to modelling near-wall turbulence energy and stress dissipation. *Journal of Fluid Mechanics*, 459:139–166, 2002.

[17] S. Fu, C. Wang, and Y. Guo. On the minimal representation of non-linear eddy-viscosity models. *Journal of Turbulence*, 12:N47, 2011.

[18] Y. Tamaki and S. Kawai. Turbulence anisotropy effects on corner-flow separation: physics and turbulence modelling. *Journal of Fluid Mechanics*, 980:A21, 2024.